condensed matter

MDPI

Article

Double-Q Checkerboard Bubble Crystal in Centrosymmetric Tetragonal Magnets

Satoru Hayami

Graduate School of Science, Hokkaido University, Sapporo 060-0810, Japan; hayami@phys.sci.hokudai.ac.jp

Abstract: We report our numerical studies on the emergence of a double-Q checkerboard bubble crystal in centrosymmetric tetragonal magnets. The double-Q checkerboard bubble crystal is characterized by a fourfold-symmetric collinear spin configuration consisting of a superposition of two sinusoidal waves with the out-of-plane spin modulations along the [110] and [$\bar{1}$10] directions. The numerical calculations based on the simulated annealing for an effective spin model with the momentum-resolved easy-axis exchange interactions reveal that the double-Q checkerboard bubble crystal is energetically degenerate with the single-Q collinear state when the ordering wave vector lies on the quarter of the reciprocal lattice vector along the $\langle 110 \rangle$ direction. We show that such a degeneracy is lifted by considering the biquadratic interaction. We also find that the double-Q checkerboard bubble crystal turns into another double-Q state characterized by the in-plane spin modulations by increasing an external magnetic field.

Keywords: bubble crystal; biquadratic interaction; multiple-Q state; square lattice; magnetic phase diagram

check for updates

Citation: Hayami, S. Double-Q Checkerboard Bubble Crystal in Centrosymmetric Tetragonal Magnets. *Condens. Matter* **2024**, *9*, 40. https://doi.org/10.3390/condmat9040040

Received: 16 August 2024
Revised: 9 October 2024
Accepted: 13 October 2024
Published: 16 October 2024

1. Introduction

Exploring unconventional magnetic orderings has been one of the central issues in condensed matter physics. Depending on the spin configurations, various intriguing physical phenomena occur, such as the anomalous Hall effect in ferromagnets [1–10] and collinear antiferromagnets [11–20], spin current generation in noncollinear antiferromagnets [21–28], and the nonreciprocal transport in noncoplanar antiferromagnets [29–36]. The findings of unconventional magnetic orderings and their related physical phenomena can not only provide fundamental understandings but also bring about future electronic and spintronic device applications [37–39].

The magnetic orderings can be described by a superposition of spin density waves, where the spin at site i, $\boldsymbol{S}_i$, is generally expressed as

$$\boldsymbol{S}_i = \sum_{\nu=1}^{n} (e^{i\boldsymbol{Q}_\nu \cdot \boldsymbol{r}_i} \boldsymbol{S}_{\boldsymbol{Q}_\nu} + e^{-i\boldsymbol{Q}_\nu \cdot \boldsymbol{r}_i} \boldsymbol{S}_{-\boldsymbol{Q}_\nu}). \tag{1}$$

Here, $\boldsymbol{S}_{\boldsymbol{q}}$ with the wave vector $\boldsymbol{q}$ is the Fourier transform of $\boldsymbol{S}_i$, and $\boldsymbol{r}_i$ is the position vector at site i. For $n = 1$, the spin state is referred to as the single-Q state, while it is referred to as the multiple-Q state for $n > 1$ [40–43]. The multiple-Q spin configurations can describe a variety of complicated spin configurations, such as a skyrmion crystal [44–51], hedgehog crystal [52–57], meron–antimeron crystal [58–62], and vortex crystal [63–67]. For example, a double-Q superposition of spiral waves leads to the skyrmion crystal on a two-dimensional square lattice and a triple-Q superposition of spiral waves leads to the hedgehog crystal on a three-dimensional cubic lattice. Since the resultant multiple-Q spin configurations depend on the type of the constituent spin density waves, further exotic magnetic orderings can be expected.

In the present study, we explore a further multiple-Q state and its stabilization mechanism based on the spin model analysis. We perform the simulated annealing for the spin

model on the two-dimensional centrosymmetric square lattice and construct the magnetic phase diagram at low temperatures. By changing an easy-axis anisotropic interaction and an external magnetic field, we find that the energy of the double-Q state is the same as that of the single-Q state within the bilinear exchange interaction. The infinitesimally small biquadratic interaction stabilizes two types of the double-Q states depending on the magnetic field. In the small field region, a double-Q checkerboard bubble crystal (2Q CBX), which consists of double-Q sinusoidal waves with the z-spin modulation, appears without the uniform magnetization, while a double-Q state with xy-spin modulations (2Q I state) appears in the high-field region. Our results indicate a possibility of further multiple-Q states by considering the interplay between the biquadratic interaction and magnetic field.

The rest of this paper is organized as follows: In Section 2, we construct an effective spin model on the square lattice to induce the 2Q CBX by taking into account the momentum-resolved spin interactions. We also introduce the simulated annealing, which enables us to obtain the thermodynamic spin configurations in an unbiased way. In Section 3, we discuss the stability of the 2Q CBX by changing the model parameters. First, we show that the energy of the 2Q CBX is degenerate with that of the 1Q collinear state within the easy-axis anisotropic bilinear exchange interaction. Then, we show that the biquadratic interaction favors the 2Q CBX rather than the 1Q collinear state. Finally, we present the magnetic phase diagram against the external magnetic field. Section 4 is devoted to the conclusion of the present paper.

2. Model and Method

We analyze the following spin model with the momentum-resolved interaction on the two-dimensional square lattice, whose Hamiltonian is given by

$$\mathcal{H} = -2\sum_{\nu}\left(J\Gamma_{\boldsymbol{Q}_\nu} + \frac{K}{N}\Gamma^2_{\boldsymbol{Q}_\nu}\right) - H\sum_i S^z_i, \tag{2}$$

with

$$\Gamma_{\boldsymbol{Q}_\nu} = \boldsymbol{S}_{\boldsymbol{Q}_\nu}\cdot\boldsymbol{S}_{-\boldsymbol{Q}_\nu} + I^z S^z_{\boldsymbol{Q}_\nu} S^z_{-\boldsymbol{Q}_\nu}, \tag{3}$$

where $\boldsymbol{S}_{\boldsymbol{Q}_\nu}$ denotes the $\boldsymbol{Q}_\nu$ component of the spin and ν is the index of the ordering wave vectors $\boldsymbol{Q}_\nu$. $\boldsymbol{S}_{\boldsymbol{Q}_\nu} = (S^x_{\boldsymbol{Q}_\nu}, S^y_{\boldsymbol{Q}_\nu}, S^z_{\boldsymbol{Q}_\nu})$ is related to the localized spin at site i, $\boldsymbol{S}_i = (S^x_i, S^y_i, S^z_i)$, via the Fourier transformation. We set the spin length as unity, i.e., $|\boldsymbol{S}_i| = 1$.

The first term represents the bilinear and biquadratic exchange interactions with the coupling constants J and K, respectively; N denotes the total number of spins in the system. We take into account the interactions at particular wave vectors by supposing the nesting of the Fermi surface at $\boldsymbol{Q}_\nu$; we set $\boldsymbol{Q}_1 = (\pi/2, \pi/2)$ and $\boldsymbol{Q}_2 = (-\pi/2, \pi/2)$; and the lattice constant is set to be unity. It is noted that the coupling constants J and K are common for $\boldsymbol{Q}_1$ and $\boldsymbol{Q}_2$, since they are connected by the fourfold rotational symmetry of the square lattice. The prefactor 2 is due to the contribution from $-\boldsymbol{Q}_1$ and $-\boldsymbol{Q}_2$. In the nesting regime, the bilinear exchange interaction corresponds to the Ruderman–Kittel–Kasuya–Yosida (RKKY) interaction [68–70], while the biquadratic exchange interaction corresponds to the higher-order RKKY interaction [71,72]. Microscopically, the RKKY (higher-order RKKY) interaction is obtained in the lowest-order (second-lowest-order) perturbative expansions with respect to the spin–charge coupling in the Kondo lattice model. The bilinear exchange interaction tends to favor the single-Q state at $\boldsymbol{Q}_\nu$, while the biquadratic interaction tends to favor the multiple-Q state, such as the vortex crystal [73], bubble crystal [74], and the higher-order skyrmion crystal [75]. In addition, we introduce the dimension-less easy-axis anisotropic form factor in $\Gamma_{\boldsymbol{Q}_\nu}$ as $I^z > 0$, while we neglect other symmetry-allowed magnetic anisotropic form factors, such as the bond-dependent magnetic anisotropy [76]. Such magnetic anisotropy in both two-spin and four-spin interactions originates from the interplay between the spin–orbit coupling and crystalline electric field; in particular, the easy-axis anisotropy arises from the inequivalence between the xy- and z-spin com-

ponents. Although we choose the same ratio of the interactions between the xy and z components for the bilinear and biquadratic interactions, the following results are not altered even for different interaction ratios in the xy and z components of the biquadratic interaction, since the biquadratic interaction is introduced to lift the degeneracy between the single-Q and double-Q states detailed in Section 3 in the present study. The second term stands for the effect of the external magnetic field along the out-of-plane direction; H represents the magnitude of the magnetic field.

We examine the instability toward the multiple-Q states by numerically solving the model in Equation (2). Although the model includes only a few interactions in momentum space, it gives an almost accurate internal energy for the ground-state spin configurations when the interactions at the other wave vectors are smaller than those at $\boldsymbol{Q}_1$ and $\boldsymbol{Q}_2$. In other words, the effective momentum-resolved spin model enables us to efficiently search for the multiple-Q states [77,78]. Such a simplification is especially useful for the examination of the instability toward the multiple-Q states in the ground state, since the ground-state energy is determined by the dominant multiple-Q (or single-Q) modulations, and the contribution from the higher-harmonic wave vectors like $\boldsymbol{Q}_1 + \boldsymbol{Q}_2$ is negligible [79]. Indeed, the simplification of the model can capture the essential interactions in materials hosting multiple-Q magnetic orderings, such as EuPtSi [80], $GdRu_2Si_2$ [81], and $EuNiGe_3$ [82], where the experimental complicated phase diagrams are well reproduced. Meanwhile, the simplification of the model does not capture unconventional multiple-Q states, whose ordering wave vectors are not symmetry-related. In addition, the model with the momentum-resolved interaction is not appropriate for the analysis of the impurity effect. In the following, we set $J = 1$ as the energy unit of the model, and change I^z and H. For K, we set $K = 0$ or $K = 0.05$, since infinitesimally small K is enough to lift the degeneracy between the single-Q and multiple-Q states.

The magnetic phase diagram is calculated in the plane of I^z and H based on the simulated annealing. For the system size with $N = 16^2$ under the periodic boundary conditions, we perform the Monte Carlo simulations with standard metropolis local updates in real space from a high temperature, $T_0 = 1.5$, to the final temperature, $T = 0.0001$. In the simulations, we flip the spin in real space according to the Metropolis algorithm. Then, we evaluate the Fourier transform of the spins only for the $\boldsymbol{Q}_1$ and $\boldsymbol{Q}_2$ components in order to evaluate the energy of the model in Equation (2). Starting from a random spin configuration at T_0, we gradually reduce the temperature with a rate of $T_{n+1} = 0.999999T_n$ while performing the above procedure, where T_n is the nth-step temperature. When the temperature reaches T, we perform 10^5–10^6 Monte Carlo sweeps for measurements. In addition, the simulations are performed from the spin configurations obtained at low temperatures in the vicinity of the phase boundaries in order to avoid the meta-stable solution. We independently perform the above procedure for a set of I^z and H.

We calculate the following physical quantities in order to identify magnetic phases obtained by the simulated annealing. The spin structure factor is given by

$$S_s(\boldsymbol{q}) = \frac{1}{N}\sum_{i,j}(\boldsymbol{S}_i \cdot \boldsymbol{S}_j)e^{i\boldsymbol{q}\cdot(\boldsymbol{r}_i-\boldsymbol{r}_j)}, \tag{4}$$

where $\boldsymbol{q}$ is the wave vector in the first Brillouin zone. The net magnetization along the magnetic field direction is given by

$$M^z = \frac{1}{N}\sum_i S_i^z. \tag{5}$$

3. Results

We discuss the multiple-Q instability in the model in Equation (2). First, we discuss the result without the biquadratic interaction in Section 3.1, where the single-Q and double-Q

states are energetically degenerate with each other. Then, we introduce the biquadratic interaction to lift such a degeneracy in Section 3.2.

3.1. Without Biquadratic Interaction

Let us discuss the case without the biquadratic interaction, i.e., $K = 0$. For $I^z = 0$, the single-Q state with the up–up–down–down spin configuration is realized in the ground state. We deduce the spin ansatz satisfying the local spin length constraint for the spin configurations obtained by the simulated annealing. In the case of $H = 0$, one of the expressions of this spin configuration is given by

$$S_i^x = S_i^y = \frac{1}{\sqrt{2}}(\cos \boldsymbol{Q}_1 \cdot \boldsymbol{r}_i - \sin \boldsymbol{Q}_1 \cdot \boldsymbol{r}_i),\ S_i^z = 0, \tag{6}$$

where we assume that the spin oscillates along the [110] direction. This spin configuration leads to the lowest energy of the model Hamiltonian, $-J = -1$, under the constraint of the spin length $|\boldsymbol{S}_i| = 1$.

Meanwhile, we find that the double-Q spin configuration gives the same lowest energy as the above single-Q state. By considering the superposition of two spin density waves at $\boldsymbol{Q}_1$ and $\boldsymbol{Q}_2$ while the local spin length is kept, the spin ansatz for the double-Q state is given as follows:

$$\begin{aligned} S_i^x &= c_1 \cos \boldsymbol{Q}_1 \cdot \boldsymbol{r}_i - \sqrt{1 - c_1^2} \sin \boldsymbol{Q}_2 \cdot \boldsymbol{r}_i, \\ S_i^y &= -c_1 \sin \boldsymbol{Q}_1 \cdot \boldsymbol{r}_i + \sqrt{1 - c_1^2} \cos \boldsymbol{Q}_2 \cdot \boldsymbol{r}_i, \\ S_i^z &= 0, \end{aligned} \tag{7}$$

where $0 < c_1 < 1$ is the numerical coefficient. The same energy between the single-Q and double-Q states is unnderstood from the fact that the spin pattern in Equation (7) satisfies the local spin constraint as $|\boldsymbol{S}_i| = 1$, owing to the special value of the ordering wave vectors $\boldsymbol{Q}_1 = (\pi/2, \pi/2)$ and $\boldsymbol{Q}_2 = (-\pi/2, \pi/2)$. In other words, all the intensities in the spin structure factor lie at $\boldsymbol{Q}_1$ and $\boldsymbol{Q}_2$ rather than the higher-harmonic wave vector like $\boldsymbol{Q}_1 + \boldsymbol{Q}_2$ and other wave vectors. This indicates no energy loss in terms of the exchange energy compared to the single-Q state, which leads to the energy degeneracy between the single-Q and double-Q states. Such a situation also holds for nonzero H. A similar energy degeneracy has been found at particular ordering wave vectors like $\boldsymbol{Q} = (\pi, 0)$ [72,83] and $\boldsymbol{Q} = (5\pi/8, 3\pi/8)$. Thus, the magnetic states with arbitrary c_1 are obtained after the simulated annealing. We show the real-space spin configurations in the left panels of Figure 1a,b. Although the spin configurations in Figure 1a,b seem to be completely different from each other, both are described by the expression in Equation (7) and their energy is given by $-J[1 - (M^z)^2] + HM^z$, which takes the same value as the single-Q state. The corresponding spin structure factors are shown in the right panels of Figure 1a,b; all the intensities are found at $\boldsymbol{Q}_1$, $\boldsymbol{Q}_2$, and $\boldsymbol{q} = \boldsymbol{0}$.

When I^z is introduced, the energy degeneracy between the single-Q state and the double-Q state also holds. At zero field, both single-Q and double-Q states are characterized by the collinear spin configurations with the z-spin component in order to gain the energy by I^z. The single-Q spin configuration is given by

$$S_i^x = S_i^y = 0,\ S_i^z = \cos \boldsymbol{Q}_1 \cdot \boldsymbol{r}_i - \sin \boldsymbol{Q}_1 \cdot \boldsymbol{r}_i, \tag{8}$$

and the double-Q spin configuration is given by

$$S_i^x = S_i^y = 0,\ S_i^z = \sin \boldsymbol{Q}_1 \cdot \boldsymbol{r}_i + \cos \boldsymbol{Q}_2 \cdot \boldsymbol{r}_i. \tag{9}$$

We show the real-space spin configuration of the double-Q state in the left panel of Figure 1c and that of the single-Q state in the left panel of Figure 1d. Their spin structure factors are

shown in the right panels of Figure 1c,d. For the double-Q state, the up and down spins form the 2×2 squares, and they are aligned in a way that resembles a checkerboard. We refer to this state as the $2Q$ CBX. A similar CBX has also been found in the tetragonal model with the different ordering wave vectors; in contrast to the present CBX state, another CBX state in the previous study was characterized by the quadruple-Q superposition at $\boldsymbol{Q}'_1 = (\pi/4, 3\pi/4)$, $\boldsymbol{Q}'_2 = (3\pi/4, -\pi/4)$, $\boldsymbol{Q}'_3 = (3\pi/4, \pi/4)$ and $\boldsymbol{Q}'_4 = (-\pi/4, 3\pi/4)$. In this way, various types of the single-Q and double-Q states are energetically degenerate within the bilinear exchange interaction for $\boldsymbol{Q}_1 = (\pi/2, \pi/2)$ and $\boldsymbol{Q}_2 = (-\pi/2, \pi/2)$.

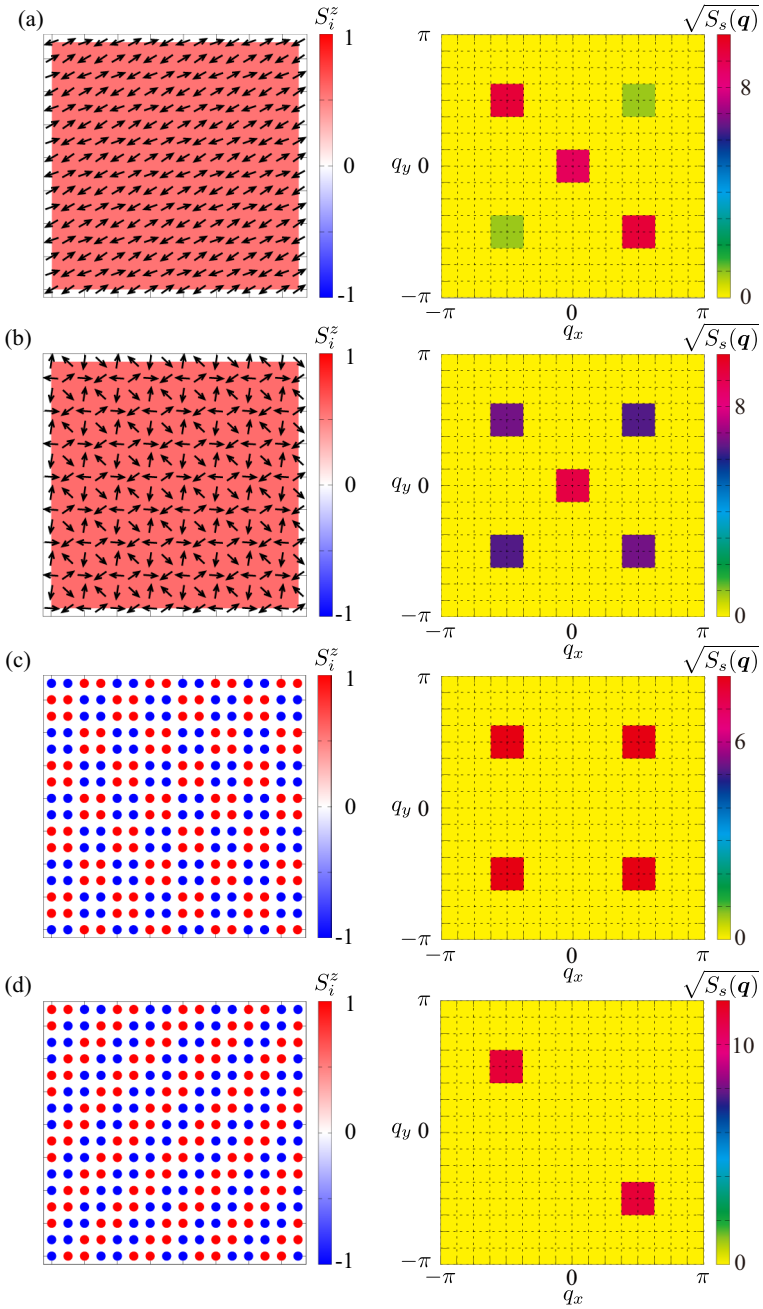

Figure 1. (**Left panel**) Real-space spin configurations of (**a**) the anisotropic double-Q state at $I^z = 0$ and $H = 1.1$, (**b**) the isotropic double-Q state at $I^z = 0$ and $H = 1.15$, (**c**) the $2Q$ CBX state at $I^z = 0.4$ and $H = 0$, and (**d**) the $1Q$ collinear state at $I^z = 0.4$ and $H = 0.05$. In (**a**,**b**), the arrows represent the directions of the spin moments and the contour shows the z-spin component. In (**c**,**d**), the color of the circles represents the z-spin component; there are no x- and y-spin components. (**Right panel**) Square root of the spin structure factor corresponding to the left panel.

3.2. With Biquadratic Interaction

In order to lift the degeneracy between the single-Q and double-Q states, we take into account the effect of the biquadratic interaction K. Since positive K tends to lead to the energy loss for the single-Q state compared to the multiple-Q state [71,72], the stabilization of the double-Q state is expected. Meanwhile, negative K tends to stabilize the single-Q state rather than the multiple-Q state. Accordingly, we focus on the effect of positive $K = 0.05$ in the following analysis.

Figure 2 shows the magnetic phase diagram while varying I^z and H at $K = 0.05$. There are mainly two magnetic phases except for the fully polarized state appearing for $H \gtrsim 2$. For $I^z = 0$, the double-Q spin configuration in Equation (7) is realized irrespective of H; we denote it as 2Q I in the phase diagram in Figure 2. The real-space spin configuration and spin structure factor of the 2Q I state are presented in the left and right panels of Figure 3a, respectively. In order to gain the energy by K, the intensities of the spin structure factor at $\boldsymbol{Q}_1$ and $\boldsymbol{Q}_2$ become almost equal; the isotropic double-Q state has a lower energy than the anisotropic double-Q state. The magnetization in this state exhibits the linear development against H, and continuously turns into the fully polarized state, as shown in Figure 4a.

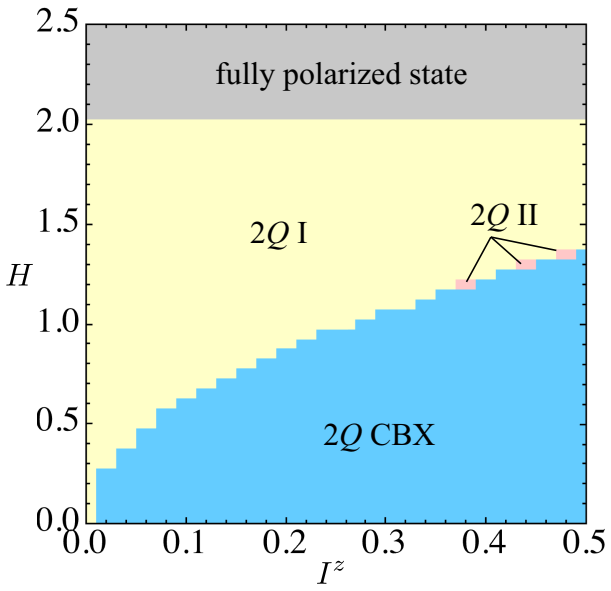

Figure 2. Magnetic phase diagram in the plane of the two-spin easy-axis anisotropic interaction I^z and the magnetic field H obtained by the simulated annealing at $K = 0.05$.

For $I^z \neq 0$, the 2Q CBX is stabilized in the low-field region, which indicates that the energy of the 2Q CBX is lower than that of the single-Q collinear state in the presence of K. The real-space spin configuration and spin structure factor are shown in Figure 3b, which are the same as those in Figure 1c. When H increases, the magnetization remains zero in the 2Q CBX, as shown in the case of $I^z = 0.1$ in Figure 4b. With a further increase in H, the 2Q CBX changes into the 2Q I state with a jump of M at $H \simeq 0.6$. This first-order phase transition is regarded as the spin–flop transition, where the spin moments are flopped from the parallel direction to the perpendicular direction in terms of the magnetic field. For larger I^z, the region where the 2Q CBX is stabilized becomes wider, and then, the magnetization jump becomes larger, as shown in the case of $I^z = 0.3$ in Figure 4c and $I^z = 0.48$ in Figure 4d.

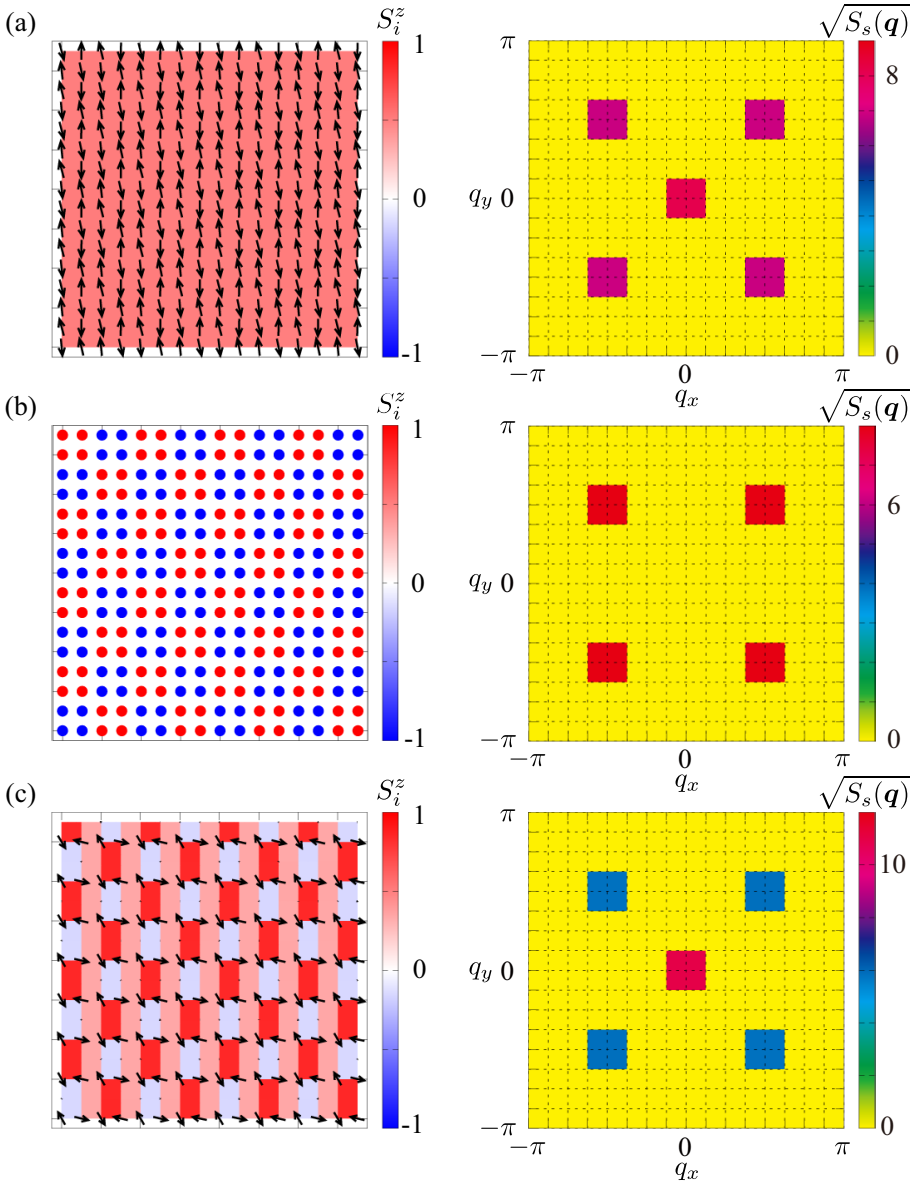

Figure 3. (**Left panel**) Real-space spin configurations of (**a**) the 2Q I state at $I^z = 0.1$ and $H = 1.0$, (**b**) the 2Q CBX at $I^z = 0.1$ and $H = 0.3$, and (**c**) the 2Q II state at $I^z = 0.48$ and $H = 1.35$. In (**a**,**c**), the arrows represent the directions of the spin moments and the contour shows the z-spin component. In (**b**), the color of the circles represents the z-spin component; there are no x- and y-spin components. (**Right panel**) Square root of the spin structure factor corresponding to the left panel.

Finally, let us comment on the intermediate magnetic phase (2Q II) appearing in the narrow region sandwiched by the 2Q CBX and 2Q I state for large I^z, as shown in Figure 2. This state is characterized by the isotropic double-Q superposition in both xy- and z-spin components like the magnetic skyrmion; the isotropic double-Q feature is found in the spin structure factor in the right panel of Figure 3c. Meanwhile, the spin configuration does not exhibit the scalar spin chirality corresponding to the topological charge, which means that the 2Q II state is topologically trivial in contrast to the magnetic skyrmion. We show the real-space spin configuration of the 2Q II state in the left panel of Figure 3c; there is no vortex with the nonzero winding number. The magnetization in this state takes almost the median value between the 2Q CBX and 2Q I states, as shown in Figure 4d, which indicates that two first-order phase transitions occur when the 2Q II state appears.

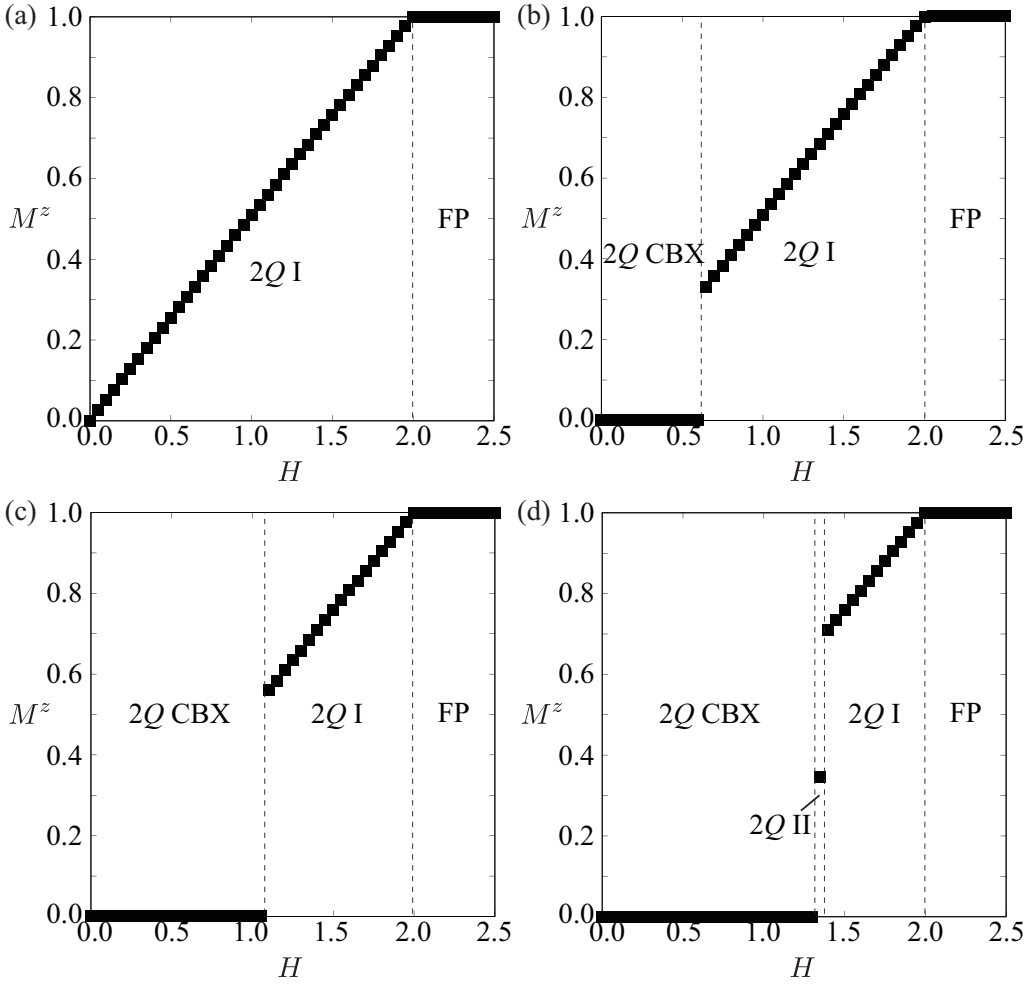

Figure 4. H dependence of the magnetization M^z at (**a**) $I^z = 0$, (**b**) $I^z = 0.1$, (**c**) $I^z = 0.3$, and (**d**) $I^z = 0.48$. The vertical dashed lines represent the phase boundary between different magnetic phases. FP represents the fully polarized state.

4. Conclusions

We have investigated the instability toward a new type of multiple-Q states in centrosymmetric tetragonal magnets by focusing on the position of the ordering wave vectors. We have shown that the single-Q and double-Q states are energetically degenerate within the easy-axis anisotropic bilinear exchange interaction and the magnetic field when the ordering wave vectors lie on $(\pi/2, \pi/2)$ and $(-\pi/2, \pi/2)$. By performing the simulated annealing and constructing the magnetic phase diagram, we have found that two types of the double-Q states, i.e., 2Q CBX and 2Q I state, are mainly realized in the presence of the biquadratic interaction. In particular, the low-field phase corresponds to the 2Q CBX state characterized by the double-Q collinear spin texture without a net magnetization. We have also found that another double-Q state denoted as 2Q II appears in the narrow region sandwiched by the low-field 2Q CBX and high-field 2Q I states. The present results indicate that the position of the ordering wave vectors might lead to further intriguing multiple-Q states distinct from the magnetic skyrmion and other well-known multiple-Q states.

Funding: This research was supported by JSPS KAKENHI, Grant Numbers JP21H01037, JP22H00101, JP22H01183, JP23H04869, JP23K03288, and JP23K20827, and by JST CREST (JPMJCR23O4).

Data Availability Statement: The original contributions presented in this study are included in the article; further inquiries can be directed to the corresponding author.

Conflicts of Interest: The author declares no conflicts of interest.

References

1. Karplus, R.; Luttinger, J.M. Hall Effect in Ferromagnetics. *Phys. Rev.* **1954**, *95*, 1154–1160. [CrossRef]
2. Smit, J. The spontaneous Hall effect in ferromagnetics II. *Physica* **1958**, *24*, 39–51. [CrossRef]
3. Maranzana, F.E. Contributions to the Theory of the Anomalous Hall Effect in Ferro- and Antiferromagnetic Materials. *Phys. Rev.* **1967**, *160*, 421–429. [CrossRef]
4. Berger, L. Side-Jump Mechanism for the Hall Effect of Ferromagnets. *Phys. Rev. B* **1970**, *2*, 4559–4566. [CrossRef]
5. Nozieres, P.; Lewiner, C. A simple theory of the anomalous Hall effect in semiconductors. *J. Phys.* **1973**, *34*, 901–915. [CrossRef]
6. Ye, J.; Kim, Y.B.; Millis, A.J.; Shraiman, B.I.; Majumdar, P.; Tešanović, Z. Berry Phase Theory of the Anomalous Hall Effect: Application to Colossal Magnetoresistance Manganites. *Phys. Rev. Lett.* **1999**, *83*, 3737–3740. [CrossRef]
7. Jungwirth, T.; Niu, Q.; MacDonald, A.H. Anomalous Hall Effect in Ferromagnetic Semiconductors. *Phys. Rev. Lett.* **2002**, *88*, 207208. [CrossRef] [PubMed]
8. Haldane, F.D.M. Berry Curvature on the Fermi Surface: Anomalous Hall Effect as a Topological Fermi-Liquid Property. *Phys. Rev. Lett.* **2004**, *93*, 206602. [CrossRef]
9. Nagaosa, N.; Sinova, J.; Onoda, S.; MacDonald, A.H.; Ong, N.P. Anomalous Hall effect. *Rev. Mod. Phys.* **2010**, *82*, 1539–1592. [CrossRef]
10. Xiao, D.; Chang, M.C.; Niu, Q. Berry phase effects on electronic properties. *Rev. Mod. Phys.* **2010**, *82*, 1959–2007. [CrossRef]
11. Solovyev, I.V. Magneto-optical effect in the weak ferromagnets $LaMO_3$ (M = Cr, Mn, and Fe). *Phys. Rev. B* **1997**, *55*, 8060–8063. [CrossRef]
12. Sivadas, N.; Okamoto, S.; Xiao, D. Gate-Controllable Magneto-optic Kerr Effect in Layered Collinear Antiferromagnets. *Phys. Rev. Lett.* **2016**, *117*, 267203. [CrossRef] [PubMed]
13. Šmejkal, L.; González-Hernández, R.; Jungwirth, T.; Sinova, J. Crystal time-reversal symmetry breaking and spontaneous Hall effect in collinear antiferromagnets. *Sci. Adv.* **2020**, *6*, eaaz8809. [CrossRef]
14. Yamasaki, Y.; Nakao, H.; Arima, T.H. Augmented Magnetic Octupole in Kagomé 120-degree Antiferromagnets Detectable via X-ray Magnetic Circular Dichroism. *J. Phys. Soc. Jpn.* **2020**, *89*, 083703. [CrossRef]
15. Naka, M.; Hayami, S.; Kusunose, H.; Yanagi, Y.; Motome, Y.; Seo, H. Anomalous Hall effect in κ-type organic antiferromagnets. *Phys. Rev. B* **2020**, *102*, 075112. [CrossRef]
16. Hayami, S.; Kusunose, H. Essential role of the anisotropic magnetic dipole in the anomalous Hall effect. *Phys. Rev. B* **2021**, *103*, L180407. [CrossRef]
17. Chen, H. Electronic chiralization as an indicator of the anomalous Hall effect in unconventional magnetic systems. *Phys. Rev. B* **2022**, *106*, 024421. [CrossRef]
18. Naka, M.; Motome, Y.; Seo, H. Anomalous Hall effect in antiferromagnetic perovskites. *Phys. Rev. B* **2022**, *106*, 195149. [CrossRef]
19. Lei, C.; Trevisan, T.V.; Heinonen, O.; McQueeney, R.J.; MacDonald, A.H. Quantum anomalous Hall effect in perfectly compensated collinear antiferromagnetic thin films. *Phys. Rev. B* **2022**, *106*, 195433. [CrossRef]
20. Gonzalez Betancourt, R.D.; Zubáč, J.; Gonzalez-Hernandez, R.; Geishendorf, K.; Šobáň, Z.; Springholz, G.; Olejník, K.; Šmejkal, L.; Sinova, J.; Jungwirth, T.; et al. Spontaneous Anomalous Hall Effect Arising from an Unconventional Compensated Magnetic Phase in a Semiconductor. *Phys. Rev. Lett.* **2023**, *130*, 036702. [CrossRef]
21. Katsura, H.; Nagaosa, N.; Balatsky, A.V. Spin Current and Magnetoelectric Effect in Noncollinear Magnets. *Phys. Rev. Lett.* **2005**, *95*, 057205. [CrossRef] [PubMed]
22. Mostovoy, M. Ferroelectricity in Spiral Magnets. *Phys. Rev. Lett.* **2006**, *96*, 067601. [CrossRef] [PubMed]
23. Sergienko, I.A.; Dagotto, E. Role of the Dzyaloshinskii-Moriya interaction in multiferroic perovskites. *Phys. Rev. B* **2006**, *73*, 094434. [CrossRef]
24. Harris, A.B.; Yildirim, T.; Aharony, A.; Entin-Wohlman, O. Towards a microscopic model of magnetoelectric interactions in $Ni_3V_2O_8$. *Phys. Rev. B* **2006**, *73*, 184433. [CrossRef]
25. Tokura, Y.; Seki, S.; Nagaosa, N. Multiferroics of spin origin. *Rep. Prog. Phys.* **2014**, *77*, 076501. [CrossRef]
26. Cardias, R.; Szilva, A.; Bezerra-Neto, M.; Ribeiro, M.; Bergman, A.; Kvashnin, Y.O.; Fransson, J.; Klautau, A.; Eriksson, O.; Nordström, L. First-principles Dzyaloshinskii–Moriya interaction in a non-collinear framework. *Sci. Rep.* **2020**, *10*, 20339. [CrossRef]
27. Lee, S.H.; Qian, Y.; Yang, B.J. Fermi Surface Spin Texture and Topological Superconductivity in Spin-Orbit Free Noncollinear Antiferromagnets. *Phys. Rev. Lett.* **2024**, *132*, 196602. [CrossRef] [PubMed]
28. Brekke, B.; Sukhachov, P.; Giil, H.G.; Brataas, A.; Linder, J. Minimal models and transport properties of unconventional *p*-wave magnets. *arXiv* **2024**, arXiv:2405.15823.
29. Seki, S.; Okamura, Y.; Kondou, K.; Shibata, K.; Kubota, M.; Takagi, R.; Kagawa, F.; Kawasaki, M.; Tatara, G.; Otani, Y.; et al. Magnetochiral nonreciprocity of volume spin wave propagation in chiral-lattice ferromagnets. *Phys. Rev. B* **2016**, *93*, 235131. [CrossRef]
30. Giordano, A.; Verba, R.; Zivieri, R.; Laudani, A.; Puliafito, V.; Gubbiotti, G.; Tomasello, R.; Siracusano, G.; Azzerboni, B.; Carpentieri, M.; et al. Spin-Hall nano-oscillator with oblique magnetization and Dzyaloshinskii-Moriya interaction as generator of skyrmions and nonreciprocal spin-waves. *Sci. Rep.* **2016**, *6*, 36020. [CrossRef]
31. Yokouchi, T.; Hoshino, S.; Kanazawa, N.; Kikkawa, A.; Morikawa, D.; Shibata, K.; Arima, T.H.; Taguchi, Y.; Kagawa, F.; Nagaosa, N.; et al. Current-induced dynamics of skyrmion strings. *Sci. Adv.* **2018**, *4*, eaat1115. [CrossRef] [PubMed]

32. Hoshino, S.; Nagaosa, N. Theory of the magnetic skyrmion glass. *Phys. Rev. B* **2018**, *97*, 024413. [CrossRef]
33. Tokura, Y.; Nagaosa, N. Nonreciprocal responses from non-centrosymmetric quantum materials. *Nat. Commun.* **2018**, *9*, 3740. [CrossRef] [PubMed]
34. Hayami, S.; Okubo, T.; Motome, Y. Phase shift in skyrmion crystals. *Nat. Commun.* **2021**, *12*, 6927. [CrossRef]
35. Hayami, S.; Yatsushiro, M. Nonlinear nonreciprocal transport in antiferromagnets free from spin-orbit coupling. *Phys. Rev. B* **2022**, *106*, 014420. [CrossRef]
36. Eto, R.; Pohle, R.; Mochizuki, M. Low-Energy Excitations of Skyrmion Crystals in a Centrosymmetric Kondo-Lattice Magnet: Decoupled Spin-Charge Excitations and Nonreciprocity. *Phys. Rev. Lett.* **2022**, *129*, 017201. [CrossRef]
37. Žutić, I.; Fabian, J.; Das Sarma, S. Spintronics: Fundamentals and applications. *Rev. Mod. Phys.* **2004**, *76*, 323–410. [CrossRef]
38. Jungwirth, T.; Marti, X.; Wadley, P.; Wunderlich, J. Antiferromagnetic spintronics. *Nat. Nanotechnol.* **2016**, *11*, 231. [CrossRef]
39. Baltz, V.; Manchon, A.; Tsoi, M.; Moriyama, T.; Ono, T.; Tserkovnyak, Y. Antiferromagnetic spintronics. *Rev. Mod. Phys.* **2018**, *90*, 015005. [CrossRef]
40. Bak, P.; Lebech, B. "Triple-$\vec{q}$" Modulated Magnetic Structure and Critical Behavior of Neodymium. *Phys. Rev. Lett.* **1978**, *40*, 800–803. [CrossRef]
41. Shapiro, S.M.; Gurewitz, E.; Parks, R.D.; Kupferberg, L.C. Multiple-q Magnetic Structure in $CeAl_2$. *Phys. Rev. Lett.* **1979**, *43*, 1748–1751. [CrossRef]
42. Bak, P.; Jensen, M.H. Theory of helical magnetic structures and phase transitions in MnSi and FeGe. *J. Phys. C Solid State Phys.* **1980**, *13*, L881. [CrossRef]
43. Jensen, J.; Bak, P. Spin waves in triple-$\vec{q}$ structures. Application to USb. *Phys. Rev. B* **1981**, *23*, 6180–6183. [CrossRef]
44. Bogdanov, A.N.; Yablonskii, D.A. Thermodynamically stable "vortices" in magnetically ordered crystals: The mixed state of magnets. *Sov. Phys. JETP* **1989**, *68*, 101.
45. Bogdanov, A.; Hubert, A. The properties of isolated magnetic vortices. *Phys. Stat. Sol. (b)* **1994**, *186*, 527–543. [CrossRef]
46. Rößler, U.K.; Bogdanov, A.N.; Pfleiderer, C. Spontaneous skyrmion ground states in magnetic metals. *Nature* **2006**, *442*, 797–801. [CrossRef]
47. Mühlbauer, S.; Binz, B.; Jonietz, F.; Pfleiderer, C.; Rosch, A.; Neubauer, A.; Georgii, R.; Böni, P. Skyrmion lattice in a chiral magnet. *Science* **2009**, *323*, 915–919. [CrossRef]
48. Yu, X.Z.; Onose, Y.; Kanazawa, N.; Park, J.H.; Han, J.H.; Matsui, Y.; Nagaosa, N.; Tokura, Y. Real-space observation of a two-dimensional skyrmion crystal. *Nature* **2010**, *465*, 901–904. [CrossRef]
49. Heinze, S.; von Bergmann, K.; Menzel, M.; Brede, J.; Kubetzka, A.; Wiesendanger, R.; Bihlmayer, G.; Blügel, S. Spontaneous atomic-scale magnetic skyrmion lattice in two dimensions. *Nat. Phys.* **2011**, *7*, 713–718. [CrossRef]
50. Nagaosa, N.; Tokura, Y. Topological properties and dynamics of magnetic skyrmions. *Nat. Nanotechnol.* **2013**, *8*, 899–911. [CrossRef]
51. Tokura, Y.; Kanazawa, N. Magnetic Skyrmion Materials. *Chem. Rev.* **2021**, *121*, 2857. [CrossRef] [PubMed]
52. Binz, B.; Vishwanath, A. Theory of helical spin crystals: Phases, textures, and properties. *Phys. Rev. B* **2006**, *74*, 214408. [CrossRef]
53. Park, J.H.; Han, J.H. Zero-temperature phases for chiral magnets in three dimensions. *Phys. Rev. B* **2011**, *83*, 184406. [CrossRef]
54. Okumura, S.; Hayami, S.; Kato, Y.; Motome, Y. Magnetic hedgehog lattices in noncentrosymmetric metals. *Phys. Rev. B* **2020**, *101*, 144416. [CrossRef]
55. Grytsiuk, S.; Hanke, J.P.; Hoffmann, M.; Bouaziz, J.; Gomonay, O.; Bihlmayer, G.; Lounis, S.; Mokrousov, Y.; Blügel, S. Topological–chiral magnetic interactions driven by emergent orbital magnetism. *Nat. Commun.* **2020**, *11*, 511. [CrossRef]
56. Shimizu, K.; Okumura, S.; Kato, Y.; Motome, Y. Phase transitions between helices, vortices, and hedgehogs driven by spatial anisotropy in chiral magnets. *Phys. Rev. B* **2021**, *103*, 054427. [CrossRef]
57. Aoyama, K.; Kawamura, H. Hedgehog-lattice spin texture in classical Heisenberg antiferromagnets on the breathing pyrochlore lattice. *Phys. Rev. B* **2021**, *103*, 14406. [CrossRef]
58. Lin, S.Z.; Saxena, A.; Batista, C.D. Skyrmion fractionalization and merons in chiral magnets with easy-plane anisotropy. *Phys. Rev. B* **2015**, *91*, 224407. [CrossRef]
59. Yu, X.Z.; Koshibae, W.; Tokunaga, Y.; Shibata, K.; Taguchi, Y.; Nagaosa, N.; Tokura, Y. Transformation between meron and skyrmion topological spin textures in a chiral magnet. *Nature* **2018**, *564*, 95–98. [CrossRef]
60. Hayami, S.; Motome, Y. Néel- and Bloch-Type Magnetic Vortices in Rashba Metals. *Phys. Rev. Lett.* **2018**, *121*, 137202. [CrossRef]
61. Bera, S.; Mandal, S.S. Theory of the skyrmion, meron, antiskyrmion, and antimeron in chiral magnets. *Phys. Rev. Res.* **2019**, *1*, 033109. [CrossRef]
62. Hayami, S.; Yambe, R. Meron-antimeron crystals in noncentrosymmetric itinerant magnets on a triangular lattice. *Phys. Rev. B* **2021**, *104*, 94425. [CrossRef]
63. Momoi, T.; Kubo, K.; Niki, K. Possible Chiral Phase Transition in Two-Dimensional Solid ^{3}He. *Phys. Rev. Lett.* **1997**, *79*, 2081–2084. [CrossRef]
64. Kamiya, Y.; Batista, C.D. Magnetic Vortex Crystals in Frustrated Mott Insulator. *Phys. Rev. X* **2014**, *4*, 11023. [CrossRef]
65. Marmorini, G.; Momoi, T. Magnon condensation with finite degeneracy on the triangular lattice. *Phys. Rev. B* **2014**, *89*, 134425. [CrossRef]
66. Wang, Z.; Kamiya, Y.; Nevidomskyy, A.H.; Batista, C.D. Three-Dimensional Crystallization of Vortex Strings in Frustrated Quantum Magnets. *Phys. Rev. Lett.* **2015**, *115*, 107201. [CrossRef]

67. Hayami, S.; Lin, S.Z.; Kamiya, Y.; Batista, C.D. Vortices, skyrmions, and chirality waves in frustrated Mott insulators with a quenched periodic array of impurities. *Phys. Rev. B* **2016**, *94*, 174420. [CrossRef]
68. Ruderman, M.A.; Kittel, C. Indirect Exchange Coupling of Nuclear Magnetic Moments by Conduction Electrons. *Phys. Rev.* **1954**, *96*, 99–102. [CrossRef]
69. Kasuya, T. A Theory of Metallic Ferro- and Antiferromagnetism on Zener's Model. *Prog. Theor. Phys.* **1956**, *16*, 45–57. [CrossRef]
70. Yosida, K. Magnetic Properties of Cu-Mn Alloys. *Phys. Rev.* **1957**, *106*, 893–898. [CrossRef]
71. Akagi, Y.; Udagawa, M.; Motome, Y. Hidden Multiple-Spin Interactions as an Origin of Spin Scalar Chiral Order in Frustrated Kondo Lattice Models. *Phys. Rev. Lett.* **2012**, *108*, 096401. [CrossRef] [PubMed]
72. Hayami, S.; Motome, Y. Multiple-Q instability by $(d\text{-}2)$-dimensional connections of Fermi surfaces. *Phys. Rev. B* **2014**, *90*, 060402(R). [CrossRef]
73. Takagi, R.; White, J.; Hayami, S.; Arita, R.; Honecker, D.; Rønnow, H.; Tokura, Y.; Seki, S. Multiple-q noncollinear magnetism in an itinerant hexagonal magnet. *Sci. Adv.* **2018**, *4*, eaau3402. [CrossRef] [PubMed]
74. Hayami, S. Multiple-Q magnetism by anisotropic bilinear-biquadratic interactions in momentum space. *J. Magn. Magn. Mater.* **2020**, *513*, 167181. [CrossRef]
75. Hayami, S. Multiple skyrmion crystal phases by itinerant frustration in centrosymmetric tetragonal magnets. *J. Phys. Soc. Jpn.* **2022**, *91*, 023705. [CrossRef]
76. Yambe, R.; Hayami, S. Effective spin model in momentum space: Toward a systematic understanding of multiple-Q instability by momentum-resolved anisotropic exchange interactions. *Phys. Rev. B* **2022**, *106*, 174437. [CrossRef]
77. Utesov, O.I. Thermodynamically stable skyrmion lattice in a tetragonal frustrated antiferromagnet with dipolar interaction. *Phys. Rev. B* **2021**, *103*, 064414. [CrossRef]
78. Wang, Z.; Su, Y.; Lin, S.Z.; Batista, C.D. Meron, skyrmion, and vortex crystals in centrosymmetric tetragonal magnets. *Phys. Rev. B* **2021**, *103*, 104408. [CrossRef]
79. Leonov, A.O.; Mostovoy, M. Multiply periodic states and isolated skyrmions in an anisotropic frustrated magnet. *Nat. Commun.* **2015**, *6*, 8275. [CrossRef]
80. Hayami, S.; Yambe, R. Field-Direction Sensitive Skyrmion Crystals in Cubic Chiral Systems: Implication to $4f$-Electron Compound EuPtSi. *J. Phys. Soc. Jpn.* **2021**, *90*, 73705. [CrossRef]
81. Hayami, S.; Kato, Y. Widely-sweeping magnetic field–temperature phase diagrams for skyrmion-hosting centrosymmetric tetragonal magnets. *J. Magn. Magn. Mater.* **2023**, *571*, 170547. [CrossRef]
82. Singh, D.; Fujishiro, Y.; Hayami, S.; Moody, S.H.; Nomoto, T.; Baral, P.R.; Ukleev, V.; Cubitt, R.; Steinke, N.J.; Gawryluk, D.J.; et al. Transition between distinct hybrid skyrmion textures through their hexagonal-to-square crystal transformation in a polar magnet. *Nat. Commun.* **2023**, *14*, 8050. [CrossRef] [PubMed]
83. Agterberg, D.F.; Yunoki, S. Spin-flux phase in the Kondo lattice model with classical localized spins. *Phys. Rev. B* **2000**, *62*, 13816–13819. [CrossRef]